CHAPTER 3

DEVELOPMENT OF A NOVEL "BALANCED ARCH" TECHNIQUE FOR MEASURING WINDS

3.1 Introduction

The general circulation of any atmosphere is defined by the nature of the atmospheric composition, pressure, temperature, and winds as functions of altitude, latitude, longitude, time of day, and season (Zurek et al., 1992). Winds are important because they transport energy, momentum, condensable species, and radiatively important aerosols within an atmosphere (Holton, 1992). Most observations of planetary atmospheres have been made by the remote sensing of electromagnetic radiation. Atmospheric composition, pressure, and temperature all have a direct effect on the transfer of radiation, and can be inferred from such observations (Chamberlain and Hunten, 1987). Winds have only an indirect effect on radiative transfer, so are less easily measured by such techniques. On all the planets, predictions of wind speed and direction as a function of altitude, latitude, longitude, time of day, and season are constrained by far fewer measurements than the complementary predictions for other meteorological fields.

In this Chapter I develop a novel technique for measuring winds and apply it on Mars. On Mars, lower atmospheric winds have previously been constrained by several techniques:

(1) Cloud tracking on images from ground-based telescopes, Earth-orbiting telescopes, and Mars-orbiting spacecraft have provided direct measurements of

winds, but these do not have systematic latitudinal, longitudinal, and seasonal coverage, do not strongly constrain the relevant altitude, and are restricted to daytime only (Slipher, 1962; Mischna et al., 1998; Kahn, 1983).

(2) Observations of surface streaks and other aeolian geomorphological features have provided direct measurements of average wind direction, but these do not have systematic latitudinal and longitudinal coverage, do not extend above the planetary boundary layer, do not have any temporal resolution, and reveal little about the wind speed (Thomas, 1981; Greeley et al., 2000).

(3) Surface meteorology instruments, including the Viking seismometers, have provided a record of wind speed and direction with very high temporal resolution over periods from a few months to a few Mars years, but they only exist at three locations on the planet and do not extend above a couple of metres high (Nakamura and Anderson, 1979; Zurek et al., 1992; Murphy et al., 2002).

(4) Vertical profiles of horizontal wind speed and direction were obtained during the descent of the two Viking Landers to the martian surface by modelling the effects of winds on the trajectory of the spacecraft. The profiles extend from several tens of kilometres altitude to the surface. However, these measurements only exist at two latitudes, longitudes, times of day, and seasons and are very challenging to extract from the data (Euler et al., 1979).

(5) Much better spatial coverage comes from an indirect technique which applies the gradient wind approximation to vertical profiles of pressure as a function of temperature derived from infra-red spectrometers (IRIS, IRTM, TES, and THEMIS) in Mars orbit (Zurek et al., 1992; Smith et al., 2001). These have poor spatial resolution and are restricted in their latitudinal/longitudinal/time of day coverage by their orbit. For example, TES data only cover two times of day from the sun-synchronous orbit of the Mars Global Surveyor (MGS) spacecraft.

Middle and upper atmospheric winds on Mars are less well constrained:

(1) Observations of stellar occultations, such as the 1976 Epsilon Gem occultation, reveal the oblateness of the martian atmosphere at about the 70 km altitude level (Elliot et al., 1977; French and Elliot, 1979). Similar oblateness measurements from the occultation of 28 Sag by Titan in 1989 were used to constrain wind speeds, but this analysis has not been done for the Epsilon Gem/Mars occultation (Hubbard et al., 1993).

(2) Ground-based spectroscopy with high spectral resolution can measure winds by their Doppler effect on the frequency of emitted radiation (Lellouch et al., 1991). Several groups have tried to make such measurements in the past decade, but only one peer-reviewed paper has been published (Gurwell et al., 1993; Schmülling et al., 1999; Moreno et al., 2001). This bottleneck is due to the difficulty of processing such measurements. Winds measured with this technique are line-of-sight only, are restricted to the Earth-facing hemisphere, and have poor spatial resolution.

Theoretical models which predict winds in the upper atmosphere of Mars are constrained by UV airglow measurements, radio occultations of the ionosphere, and data from the Viking entry accelerometers, retarding potential analyzers, and mass spectrometers as discussed in Bougher and Dickinson (1988) and Barth et al. (1992). The underdeveloped state of our understanding of the physics and chemistry of the martian upper atmosphere was highlighted by the recent Decadal Survey recommendation for a Mars Upper Atmosphere Observer spacecraft (Belton, 2002).

In situ observations relevant to the dynamics of the martian upper atmosphere have recently been made by the Accelerometer Experiment (ACC) on the MGS spacecraft (Keating et al., 1998; Keating et al., 2001a; Keating et al., 2001b). Once in orbit around Mars, MGS's periapsis was lowered into the upper regions of the atmosphere. The subsequent atmospheric drag from this *aerobraking* modified the spacecraft trajectory more cheaply than the use of chemical propellant alone could. The ACC measured the aerodynamic accelerations on the spacecraft during an aerobraking pass. This information was used by the mission operations team in

the hours after the aerobraking pass to plan modifications to the spacecraft's trajectory by changing the altitude of the next periapsis by small expenditures of chemical propellant at apoapsis, to achieve the desired drag without exceeding heating rate thresholds, and to guide it safely to the desired mapping orbit. The accelerometer readings have been processed to generate two "profiles" of atmospheric density, one for the inbound "leg" and one for the outbound "leg", from each "aerobraking pass" (Keating et al., 1998; Cancro et al., 1998; Tolson et al., 1999; Tolson et al., 2000; Keating et al., 2001a; Keating et al., 2001b). An "aerobraking pass" refers to a single traverse through the atmosphere from ingress to egress, a "leg" refers to the inbound (pre-periapsis) or outbound (post-periapsis) portion of an aerobraking pass, and a "profile" refers to data from one leg of an aerobraking pass. Unlike planetary entry probes or landers such as Pathfinder, the flight path of MGS through the atmosphere on each aerobraking pass is not near-vertical. The atmospheric flight path extends down from a maximum altitude of approximately 160 km to periapsis and then back out again, typically spanning several tens of degrees of latitude with only small changes in longitude or local solar time (LST). The maximum altitude is set by the need for the signal of the aerodynamic acceleration to exceed the instrument's noise level. The duration of each aerobraking pass was on the order of a few minutes, short compared to any dynamical timescale for changes in atmospheric properties. In an attempt to keep terminology consistent between one-legged lander entry data and two-legged aerobraking data, I use a "profile" of some type of data to mean a single-valued function of altitude.

Aerobraking took place in two Phases, 1 and 2, separated by a hiatus containing the Science Phasing Orbits (Albee et al., 1998; Albee et al., 2001). Phase 1 included orbits 1 – 201 from mid-September, 1997, to late March, 1998, and Phase 2 included orbits 574 – 1283 from mid-September, 1998, to early February, 1999. At the beginning of Phase 1, $L_s = 180°$, periapsis occurred at 30°N and 18 hrs LST, then moved northwards and earlier in the day to reach 60°N and 11 hrs LST at the end of Phase 1, $L_s = 300$. One hour of LST equals 1/24 of a martian solar day (sol), not 3600 seconds of elapsed time. At the beginning of Phase 2, during the

next martian year at $L_s = 30°$, periapsis occurred at 60°N and 17 hrs LST, then moved southwards and earlier in the day to cross 80°S at 15 hrs LST. Periapsis then crossed over the south pole, moving through nighttime LSTs, and reached 60°S and 02 hrs LST by the end of Phase 2, $L_s = 90°$. When periapsis was near the south pole, each aerobraking pass's profile of atmospheric density spanned a large range of LST and longitude. This is summarized in Figure 2.1. L_s, heliocentric longitude or season, is 0° at the northern spring equinox, 90° at the northern summer solstice, 180° at the northern autumn equinox, and 270° at the northern winter solstice.

Data from the ACC is archived in the Planetary Data System (PDS) (Keating et al., 2001a). This dataset contains 1600 upper atmospheric density profiles from 800 aerobraking passes. The only previous three atmospheric density profiles are those of the Pathfinder and two Viking landers (Magalhães et al., 1999; Seiff and Kirk, 1977a). Collocated pressure profiles were derived from these three near-vertical density profiles using the assumption that a pressure gradient and gravity are the only forces acting on the atmosphere. This is a slightly more restrictive assumption than the assumption of hydrostatic equilibrium. Hydrostatic equilibrium requires that a pressure gradient be the only force acting in a vertical direction, but permits additional forces, such as those due to atmospheric motions, acting in other directions. An equation of state, appropriate for the independently known atmospheric composition, such as the ideal gas law was used to derive collocated temperature profiles from these density and pressure profiles. The temperature and pressure data are generally more scientifically useful than the density data and I have investigated whether temperature and pressure profiles can be derived from the MGS ACC density profiles. The PDS archive includes the altitude of a constant pressure level, 1.26 nbar, for both the inbound and outbound legs of each aerobraking pass, so it might be thought that some useful information on how pressure profiles can be derived would be present within the archive (Keating et al., 2001a). However, the archive does not include any description of how this pressure was calculated.

Using techniques derived from these established assumptions for each leg of each aerobraking pass, I derived two pressure profiles, inbound and outbound, for each aerobraking pass from the density profiles. Since the two simultaneous pressure profiles both terminate at the same periapsis position, they should be consistent. If the two estimates of periapsis pressure are inconsistent, then the pressure profiles cannot both be correct and I must examine the assumptions and the data for errors. If the two estimates of periapsis pressure are consistent, then the pressure profiles may or may not be correct. I found typical discrepancies of 50% between the two estimates of periapsis pressure on a given aerobraking pass, significantly greater than the uncertainty in the discrepancies. Figure 3.1 shows pressure profiles derived in this way for orbit P679. It has a discrepancy of about 30% between the two estimates of periapsis pressure with an uncertainty in this discrepancy of about 1%.

A matching pair of legs, inbound and outbound, that comprise a single aerobraking pass are required to reveal this problem with the pressure profiles. A single leg, as is obtained for all entry probes, is insufficient. As I shall later show, the problem originates in the non-vertical flight paths of each aerobraking pass. It has less of an effect on profiles from typical entry probes with near-vertical flight paths.

I attribute these discrepancies to the presence of horizontal pressure gradients, which are often associated with winds. These discrepancies are the motivation for the aim of this chapter, which is to study theoretically the effects of winds and horizontal pressure gradients on density profiles from aerobraking or similar measurements.

3.2 Conservation of Momentum in an Atmosphere

$$\frac{\partial \underline{v}}{\partial t} + (\underline{v}.\underline{\nabla})\,\underline{v} + 2\underline{\Omega} \times \underline{v} + \nu_{ni}\left(\underline{v} - \underline{V}_i\right) + \frac{1}{\rho}\underline{\nabla} \times (\eta\underline{\nabla} \times \underline{v}) = \frac{-1}{\rho}\underline{\nabla}p + \underline{g}_{eff} \quad (3.1)$$
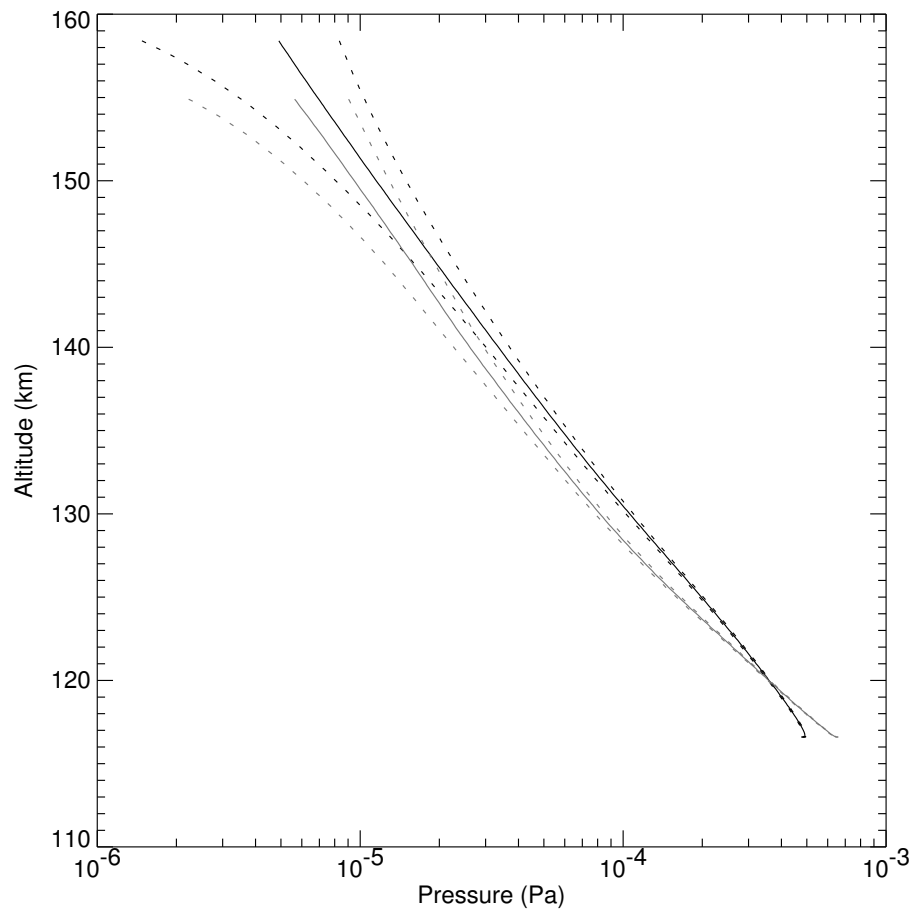
Figure 3.1: Pressure profiles derived for orbit P679 using established assumptions. The inbound profile is the solid black line, the outbound profile is the solid grey line. 1σ uncertainties for both are shown as dotted lines.

Equation 3.1, where $\underline{v}$ is the neutral wind velocity, t is universal time, $\underline{\Omega}$ is the planetary sidereal rotation rate, ν_{ni} is the neutral-ion collision frequency, $\underline{V_i}$ is the ion velocity, ρ is atmospheric density, η is the molecular dynamic viscosity, p is atmospheric pressure, and $\underline{g_{eff}}$ is the sum of gravitational and centrifugal accelerations, conserves momentum in an atmosphere in a planet-fixed rotating reference frame. This equation is discussed in $e.$ $g.$ Holton (1992) or Chamberlain and Hunten (1987).

The first term on the left hand side of Equation 3.1 is the acceleration term, the second is the advective term, the third is the Coriolis term, the fourth is the ion-drag term, and the fifth is the viscous term. The first term on the right hand side of Equation 3.1 is the pressure gradient term and the second is the gravitational term. In a static ($\underline{v} = \underline{0}$, $\underline{V_i} = \underline{0}$) atmosphere, the left hand side of Equation 3.1 is zero and pressure gradient forces are exactly balanced by the effective (including centrifugal) force of gravity.

$$\underline{g_{eff}} = \underline{g_{grav}} - \underline{\Omega} \times (\underline{\Omega} \times \underline{r}) \qquad (3.2)$$

Equation 3.2 defines $\underline{g_{eff}}$. The true gravitational acceleration, dependent only on the mass distribution within the planet, is $\underline{g_{grav}}$, the centrifugal acceleration is $-\underline{\Omega} \times (\underline{\Omega} \times \underline{r})$, and $\underline{r}$ is the position vector measured from the centre of mass of the planet. For a spherically symmetric planet, $\underline{g_{grav}}$ is directed radially. For a real planet, the spherical symmetry may be broken by terms of higher degree and order. The largest contributor to $\underline{g_{eff}}$ is always the spherically symmetric term, $-GM/r^2$ where G is the gravitational constant, M is the mass of the planet and $r = |\underline{r}|$

3.2.1 Simplest Approximation to Equation 3.1

The radial component of the acceleration due to $\underline{g_{eff}}$ is always much greater than the two perpendicular components; if it were not, then the planet's atmosphere

would rapidly escape into space. Maxwellian molecular speeds in a planetary atmosphere are simply too small for the velocity-dependent terms on the left hand side of Equation 3.1 to balance this large acceleration, so the radial pressure gradient term must balance it. This reasoning leads to the following approximation to Equation 3.1:

$$0 = \frac{-1}{\rho}\frac{\partial p}{\partial r} + \frac{-GM}{r^2} \tag{3.3}$$

$$0 = \frac{-1}{\rho}\frac{\partial p}{\partial \theta} \tag{3.4}$$

$$0 = \frac{-1}{\rho}\frac{\partial p}{\partial \phi} \tag{3.5}$$

where θ is colatitude and ϕ is east longitude. This spherical polar coordinate system is centred on the planet's centre of mass. Using the known GM, a boundary condition, and a radial profile of density as a function of altitude, Equation 3.3 can be integrated to obtain a collocated profile of pressure. The boundary condition, which is usually applied at the top of the atmosphere, is usually the assumption of an isothermal atmosphere. The pressure at the top of the atmosphere can then be related to the observable density scale height via $p = \rho g H$. Errors in the derived pressure at this high altitude have a negligible effect on the pressure profile at lower altitudes since pressure has an exponential dependence on altitude. From the independently known atmospheric composition as a function of altitude, an equation of state can be derived and used with the pressure and density profiles to yield a collocated profile of atmospheric temperature.

Slightly more sophisticated versions of this established technique have been successfully applied to near-vertical entry profiles from many spacecraft, as discussed

in Magalhães et al. (1999). However, as discussed in Section 3.1, it fails when applied to the MGS ACC density profiles. A new formulation must be found, one that allows for the non-vertical flight path of the spacecraft and uses the new constraint of two simultaneous profiles. Similar issues were addressed by Seiff et al. (1979) in their analysis of the simultaneous entries of the Pioneer Venus probes. To identify which terms in Equation 3.1 are most important in this situation I perform a scale analysis.

3.2.2 Scale Analysis on Equation 3.1

I work in a spherical polar coordinate frame, so my latitudes and longitudes are planetocentric, rather than planetographic or some other system. I do not use altitude referenced to an equipotential surface, which is the vertical coordinate in the PDS ACC data archive, because of a desire to be rigorous and correct in my vector algebra (Keating et al., 2001a). The change in unit vectors with position would be very complicated to express analytically if a reference surface without a simple form in a Cartesian coordinate system (such as a fourth degree and order equipotential surface) was used. Many atmospheric science applications use pressure as a vertical coordinate, because this can simplify the study of certain phenomena (Holton, 1992). However, this is only true when pressure is well-known. Since the ACC data here are known as a function of position, unlike, *e. g.,* remotely-sensed TES vertical profiles of temperature which are known as functions of pressure, I use a more appropriate "position-centric" coordinate system. Doing so introduces curvature terms as discussed in Appendix C.

The three components of Equation 3.1 become:

$$
\frac{\partial v_r}{\partial t} + (\underline{v}.\underline{\nabla}) \, v_r + 2 \left(-\Omega v_\phi \sin \theta \right) - \frac{v_\theta^2 + v_\phi^2}{r} =
$$
$$
\frac{-1}{\rho} \frac{\partial p}{\partial r} + g_{eff,r} - \nu_{ni} \left(v_r - V_{i,r} \right)
$$

<div align="right">(3.6)</div>

$$\frac{\partial v_\theta}{\partial t} + (\underline{v}.\underline{\nabla}) \, v_\theta + 2 \left(-\Omega v_\phi \cos \theta \right) + \frac{v_\theta v_r}{r} - \frac{v_\phi^2}{r \tan \theta} = \tag{3.7}$$
$$\frac{-1}{\rho r} \frac{\partial p}{\partial \theta} + g_{eff,\theta} + \frac{\eta}{\rho} \frac{\partial^2 v_\theta}{\partial r^2} - \nu_{ni} \left(v_\theta - V_{i,\theta} \right)$$

$$\frac{\partial v_\phi}{\partial t} + (\underline{v}.\underline{\nabla}) \, v_\phi + 2\Omega \left(\cos \theta v_\theta + \sin \theta v_r \right) + \frac{v_\phi v_r}{r} + \frac{v_\phi v_\theta}{r \tan \theta} = \tag{3.8}$$
$$\frac{-1}{\rho r \sin \theta} \frac{\partial p}{\partial \phi} + g_{eff,\phi} + \frac{\eta}{\rho} \frac{\partial^2 v_\phi}{\partial r^2} - \nu_{ni} \left(v_\phi - V_{i,\phi} \right)$$

where

$$(\underline{v}.\underline{\nabla}) = v_r \frac{\partial}{\partial r} + \frac{v_\theta}{r} \frac{\partial}{\partial \theta} + \frac{v_\phi}{r \sin \theta} \frac{\partial}{\partial \phi} \tag{3.9}$$

The viscosity term is not included in its full complexity. Only the dominant component, as detailed in Appendix D, is included in Equations 3.7 and 3.8. The dominant viscous component in Equation 3.6 is not included, because the work of Section 3.2.1 and later in this Section show that Equation 3.6 is completely dominated by the balance between gravity and the pressure gradients. The g_{eff} terms are known *a priori*, but estimates must be made for the other terms. I do not estimate the pressure gradient terms: instead, I treat them as unknowns.

$$g_{eff,r} = -\frac{-GM}{r^2} - \frac{3GM}{r^2} \left(\frac{r_{ref}}{r} \right)^2 \sqrt{5} \left(\frac{3}{2} \cos^2 \theta - \frac{1}{2} \right) \bar{C}_{20} + r\Omega^2 \sin^2 \theta \tag{3.10}$$

$$g_{eff,\theta} = -\frac{3GM}{r^2} \left(\frac{r_{ref}}{r} \right)^2 \sqrt{5} \sin \theta \cos \theta \bar{C}_{20} + r\Omega^2 \sin \theta \cos \theta \tag{3.11}$$

$$g_{eff,\phi} = 0 \tag{3.12}$$

Equations 3.10 – 3.12 contain an expansion of the gravitational field to second degree and order. r_{ref} is a reference distance and $\bar{C}_{20}$ is the first normalized zonal harmonic coefficient. First degree and order coefficients are zero when the centre of mass is at the origin of the coordinate system. r_{ref} is often, but is not required to be, the mean equatorial radius of the planet. $\bar{C}_{20}$ has meaning only in association with this reference radius. The factor of $\sqrt{5}$ comes from the normalization convention which is discussed in Section 4.1. I work up to second degree and order so that my results do not become dependent on perfect spherical symmetry in the gravitational field, but do not go to higher order because those terms are negligible.

Typical time and length scales for changes in the neutral wind velocity are:

$$\frac{\partial}{\partial t} \sim \frac{\Omega}{2\pi} \qquad (3.13)$$

$$\frac{\partial}{\partial r} \sim \frac{1}{H} \qquad (3.14)$$

$$\frac{1}{r}\frac{\partial}{\partial \theta} \sim \frac{1}{r_{ref}} \qquad (3.15)$$

$$\frac{1}{r}\frac{\partial}{\partial \phi} \sim \frac{1}{r_{ref}} \qquad (3.16)$$

where H is an atmospheric scale height. Strictly, the horizontal length scale should be the radial distance to the region of interest. This might be significantly larger than than r_{ref}, which is most probably the planet's equatorial radius. In the cases to be discussed here, either the radial distance to the region of interest is

close to r_{ref} or $\bar{C}_{20}$ ise negligible and I can use the radial distance to the region of interest as r_{ref}. These are discussed at the appropriate times. I replace each term in Equations 3.6 – 3.8 with its likely magnitude (Equations 3.17–3.19), see which terms are dominant and which are negligible, then find reasonable approximations to these Equations using only the dominant terms.

$$\frac{v_r \Omega}{2\pi} + \frac{v_r v_r}{H} + \frac{v_\theta v_r}{r_{ref}} + \frac{v_\phi v_r}{r_{ref} \sin\theta} + \quad (3.17)$$

$$2\Omega v_\phi \sin\theta + \frac{v_\theta^2}{r_{ref}} + \frac{v_\phi^2}{r_{ref}} + \nu_{ni}\left(v_r - V_{i,r}\right) =$$

$$\frac{1}{\rho}\frac{\partial p}{\partial r} + \frac{GM}{r_{ref}^2} + \frac{3GM}{r_{ref}^2}\sqrt{5}\left(\frac{3}{2}\cos^2\theta - \frac{1}{2}\right)\bar{C}_{20} + r_{ref}\Omega^2 \sin^2\theta$$

$$\frac{v_\theta \Omega}{2\pi} + \frac{v_r v_\theta}{H} + \frac{v_\theta v_\theta}{r_{ref}} + \frac{v_\phi v_\theta}{r_{ref} \sin\theta} + \quad (3.18)$$

$$2\Omega v_\phi \cos\theta + \frac{v_\theta v_r}{r_{ref}} + \frac{v_\phi^2}{r_{ref} \tan\theta} + \nu_{ni}\left(v_\theta - V_{i,\theta}\right) =$$

$$\frac{1}{\rho r}\frac{\partial p}{\partial \theta} + \frac{3GM}{r_{ref}^2}\sqrt{5}\sin\theta\cos\theta\bar{C}_{20} + r_{ref}\Omega^2 \sin\theta\cos\theta + \frac{\eta v_\theta}{\rho H^2}$$

$$\frac{v_\phi \Omega}{2\pi} + \frac{v_r v_\phi}{H} + \frac{v_\theta v_\phi}{r_{ref}} + \frac{v_\phi v_\phi}{r_{ref} \sin\theta} + \quad (3.19)$$

$$2\Omega v_\theta \cos\theta + 2\Omega v_r \sin\theta + \frac{v_\phi v_r}{r_{ref}} + \frac{v_\phi v_\theta}{r_{ref} \tan\theta} + \nu_{ni}\left(v_\phi - V_{i,\phi}\right) =$$

$$\frac{1}{\rho r \sin\theta}\frac{\partial p}{\partial \phi} + \frac{\eta v_\phi}{\rho H^2}$$

The ion-drag term only operates if the magnetic field is strong enough to control the motion of the ions (Rees, 1989). If the ion gyrofrequency, f_{gyro}, is greater than the ion-neutral collision frequency, ν_{in}, then the motions of the ions are controlled by the magnetic field, else they are not. The ratio of the ion-neutral collision frequency (frequency of collisions of neutrals with a given ionic particle)

to the neutral-ion collision frequency (frequency of collisions of ions with a given neutral particle) equals the ratio of the neutral number density to the ion number density, so the ion-neutral collision frequency is greater than the neutral-ion collision frequency.

$$f_{gyro} = \frac{1}{2\pi} \frac{q_{ion} B}{m_{ion}} \tag{3.20}$$

$$\nu_{in} = n_{neutral} A_{neutral} \sqrt{\frac{3kT_{ion}}{m_{ion}}} \tag{3.21}$$

$$\frac{f_{gyro}}{\nu_{in}} = \frac{q_{ion}}{2\pi} \frac{1}{\sqrt{3k}} \frac{B}{n_{neutral} A_{neutral}} \frac{1}{\sqrt{m_{ion} T_{ion}}} \tag{3.22}$$

where q_{ion} is the magnitude of the ionic charge, typically the same as an electron, B is the magnetic field strength, m_{ion} is the ion mass, $n_{neutral}$ is the number density of neutral particles, $A_{neutral}$ is the cross-sectional area of a neutral particle, k is Boltzmann's constant, and T_{ion} is the temperature of the ions. If this ratio is greater than unity, then $\underline{V}_i$ differs from the neutral wind velocity $\underline{v}$ and the ion-drag term is non-zero. $\underline{V}_i$ can be estimated by assuming that the ions remain fixed on field-lines and rotate with the planet.

I perform this scale analysis for Venus, Mars, and Titan. At Venus, the Orbiter Neutral Mass Spectrometer (ONMS) of the Pioneer Venus Orbiter (PVO) measured density profiles that, like the MGS ACC, descend into and rise out of the atmosphere (Niemann et al., 1980). The compositional information from this instrument has been analysed in detail, but its dynamical implications have been less well-studied (Kasprzak et al., 1993). Relevant Mars observations come from the aerobraking of MGS, Mars Odyssey (2001 – 2002), MRO (planned for 2005 – 2006) and, depending on its operational usage, the Nozomi mass spectrometer which

arrives at Mars in 2003 (Lammer et al., 2000). At Titan, Cassini's Ion Neutral Mass Spectrometer (INMS) will measure density profiles analogously to PVO at Venus (Kasprzak et al., 1996). It is likely that similar data exist for Earth.

Now I must estimate the magnitude of each of these terms using values appropriate for the planet and dataset in question. I consider each advective term in the equations separately, unlike *e. g.* page 39 of Holton (1992). I do this in order to consider vertical, zonal, and meridional terms separately for maximum understanding of the force balances. Relevant parameters are listed in Table 3.1.

3.3   Mars Scale Analysis

Order of magnitude estimates of the parameters in Equations 3.17 – 3.19 for ACC data from MGS aerobraking are given in Table 3.1.

In this case, the radial distance to aerobraking altitudes of 100 km is not significantly different from r_{ref} for the gravitational field. I can use the gravitational field's r_{ref} as the lengthscale for some of the dynamical terms, as discussed in Section 3.2.2.

The ratio of f_{gyro} to ν_{in} is ~ 0.1, so the ion-drag term has no effect. I later show that even if this ratio is of order unity, then the ion-drag term is still negligible.

3.3.1 r component

The first row of Table 3.2 shows the magnitude of each term from Equation 3.17. The dominant term is the 3.73 m s^{-2} gravitational term. The known contributions to the gravitational effects from $\bar{C}_{20}$ and the centrifugal term are much smaller. The largest dynamical term on the left hand side of Equation 3.17 is the $1/\sin\theta$ part of the advective term at polar latitudes. Only when $\theta < 4.5° \times 10^{-3}$ does this term

Parameter	Venus (day, CO_2)	Venus (night, O)	Mars	Titan
GM (m^3 s^{-2})	3.2E14 [1]	3.2E14 [1]	4.3E13 [1]	9.0E12 [1]
$\bar{C}_{20}$ (dimless)	-2.0E-6 [2]	-2.0E-6 [2]	-8.8E-4 [1]	?
Ω (rad s^{-1})	1.2E-8 [1]	1.2E-8 [1]	7E-5 [1]	4.6E-6 [12]
r_{ref} (m)	6.2E6 [1,3]	6.2E6 [1,3]	3.4E6 [1]	3.5E6 [11]
H (m)	5E3 [3]	5E3 [3]	1E4 [8]	8E4 [12]
v_r (m s^{-1})	1 [4]	1 [4]	1 [7]	1 [13]
v_θ (m s^{-1})	5 [5]	5 [5]	30 [7]	20 [13]
v_ϕ (m s^{-1})	100 [5]	100 [5]	100 [7]	100 [13]
η (kg m^{-1} s^{-1})	1.0E-5 [6]	1.1E-5 [6]	1.0E-5 [6]	1.3E-5 [12]
ρ (kg m^{-3})	5E-10 [3]	2E-11 [3]	1E-9 [8]	8.5E-11 [12]
q_{ion} (C)	1.6E-19	1.6E-19	1.6E-19	1.6E-19
B (T)	<3E-10 [1]	<3E-10 [1]	1E-6 [9]	<1.6E-9 [10]
$n_{neutral}$ (m^{-3})	8E15 [3]	5E14 [3]	1E16 [8]	1.9E15 [12]
$A_{neutral}$ (m^2)	1E-18	1E-18	1E-18	1E-18
m_{ion} (kg)	7.3E-26 [3]	2.7E-26 [3]	7.3E-26 [1]	4.5E-26 [1]
T_{ion} (K)	280 [3]	110 [3]	200 [7,8]	200 [12]

Table 3.1: Relevant Parameters. References are: [1] Lodders and Fegley (1998); [2] National Space Science Data Center (2003); [3] Niemann et al. (1980); [4] Kerzhanovich and Marov (1983); [5] Schubert (1983); [6] Lide (1994); [7] Bougher et al. (1990); [8] Keating et al. (2001a); [9] Purucker et al. (2000); [10] Neubauer et al. (1984); [11] Yelle (pers. comm., 2002); [12] Rishbeth et al. (2000); [13] Müller-Wodarg et al. (2000)

approach 10% of the dominant 3.73 m s^{-2} gravitational term. So at all latitudes Equation 3.6 is well-approximated by:

$$0 = \frac{-1}{\rho}\frac{\partial p}{\partial r} + \frac{-GM}{r^2} \tag{3.23}$$

3.3.2 θ component

The first row of Table 3.3 shows the magnitude of each term from Equation 3.18.

The two $\sin\theta\cos\theta$ terms contributing to $g_{eff,\theta}$ are known *a priori*. The latitude-independent viscous term is not. The dominant term on the left hand side of Equation 3.18 depends on latitude as shown in Table 3.4. The competing terms are the largest latitude-independent part of the advective term, the $1/\sin\theta$ part of the advective term, the $\cos\theta$ Coriolis term, and the $1/\tan\theta$ part of the curvature term. The competing terms are symmetric about the equator.

The Coriolis term, $2\Omega v_\phi\cos\theta$, is dominant, but only by factors of a few, between $\theta = 30°$ and $\theta = 60°$, corresponding to latitudes between 30° and 60° in either hemisphere. The poleward limit is set by the curvature term, $v_\phi^2/r_{ref}\tan\theta$. The viscous term is not many times smaller than the Coriolis term, but I feel that I have underestimated the vertical lengthscale for changes in wind velocity by equating it to the scale height. There is no compelling reason for many reversals in the wind speed over the many scale heights-extent of the upper atmosphere. This reasoning suggests that neither the viscous nor largest latitude-independent part of the advective term are as large as I have outlined above. At mid-latitudes Equation 3.7 is well-approximated by:

$$-2\Omega v_\phi\cos\theta = \frac{-1}{r\rho}\frac{\partial p}{\partial \theta} + g_{eff,\theta} \tag{3.24}$$

(A)

Object	$\frac{v_r \Omega}{2\pi}$	$\frac{v_r v_r}{H}$	$\frac{v_\theta v_r}{r_{ref}}$	$\frac{v_\phi v_r}{r_{ref}\sin\theta}$
Mars	1.1×10^{-5}	10^{-4}	8.85×10^{-6}	$\frac{2.95 \times 10^{-5}}{\sin\theta}$
Venus	1.2×10^{-9}	2.0×10^{-4}	8.1×10^{-7}	$\frac{1.6 \times 10^{-5}}{\sin\theta}$
Titan	7.3×10^{-7}	1.3×10^{-5}	5.7×10^{-6}	$\frac{2.9 \times 10^{-5}}{\sin\theta}$

(B)

Object	$|2\Omega v_\phi \sin\theta|$	$\frac{v_\theta^2}{r_{ref}}$	$\frac{v_\phi^2}{r_{ref}}$
Mars	$0.014 \sin\theta$	2.6×10^{-4}	2.9×10^{-3}
Venus	$2.4 \times 10^{-6} \sin\theta$	4.0×10^{-6}	1.6×10^{-3}
Titan	$9.2 \times 10^{-4} \sin\theta$	1.1×10^{-4}	2.9×10^{-3}

(C)

Object	$\left|\frac{1}{m\,s^{-2}}\left(\frac{-1}{\rho}\frac{\partial p}{\partial r}\right)\right|$	$\frac{GM}{r_{ref}^2}$
Mars	$\frac{1}{m\,s^{-2}}\left(\frac{-1}{\rho}\frac{\partial p}{\partial r}\right)$	3.73
Venus	$\frac{1}{m\,s^{-2}}\left(\frac{-1}{\rho}\frac{\partial p}{\partial r}\right)$	8.3
Titan	$\frac{1}{m\,s^{-2}}\left(\frac{-1}{\rho}\frac{\partial p}{\partial r}\right)$	6.6×10^{-1}

(D)

Object	$\left|\frac{3GM}{r_{ref}^2}\sqrt{5}\left(\frac{3}{2}\cos^2\theta - \frac{1}{2}\right)\bar{C}_{20}\right|$	$\left|r_{ref}\Omega^2 \sin^2\theta\right|$
Mars	$0.015\left(\frac{3}{2}\cos^2\theta - \frac{1}{2}\right)$	$0.017 \sin^2\theta$
Venus	$7.4 \times 10^{-5}\left(\frac{3}{2}\cos^2\theta - \frac{1}{2}\right)$	$8.9 \times 10^{-10} \sin^2\theta$
Titan	$3.0\bar{C}_{20}\left(\frac{3}{2}\cos^2\theta - \frac{1}{2}\right)$	$7.4 \times 10^{-5} \sin^2\theta$

Table 3.2: Scale Analysis of Equation 3.6. Units are m s^{-2}. Each term in (A) and (B) corresponds to a term on the left-hand side of Equation 3.17, (C) and (D) to the right-hand side.

(A) Object	$\frac{v_\theta\Omega}{2\pi}$		$\frac{v_r v_\theta}{H}$		$\frac{v_\theta v_\theta}{r_{ref}}$		$\frac{v_\phi v_\theta}{r_{ref}\sin\theta}$
Mars	3.3×10^{-4}		3×10^{-3}		2.7×10^{-4}		$\frac{8.85\times10^{-4}}{\sin\theta}$
Venus	9.5×10^{-9}		1.0×10^{-5}		4.0×10^{-6}		$\frac{8.1\times10^{-5}}{\sin\theta}$
Titan	1.5×10^{-5}		2.5×10^{-4}		1.1×10^{-4}		$\frac{5.7\times10^{-4}}{\sin\theta}$

(B) Object	$|2\Omega v_\phi\cos\theta|$	$\left|\frac{v_\theta v_r}{r_{ref}}\right|$	$\frac{v_\phi^2}{r_{ref}\tan\theta}$
Mars	$0.014\cos\theta$	8.8×10^{-6}	$\frac{2.9\times10^{-3}}{\tan\theta}$
Venus	$2.4\times10^{-6}\cos\theta$	8.1×10^{-7}	$\frac{1.6\times10^{-3}}{\tan\theta}$
Titan	$9.2\times10^{-4}\cos\theta$	5.7×10^{-6}	$\frac{2.9\times10^{-3}}{\tan\theta}$

(C) Object	$\left|\frac{1}{m\,s^{-2}}\frac{-1}{\rho r}\frac{\partial p}{\partial\theta}\right|$	$\left|\frac{3GM}{r_{ref}^2}\sqrt{5}\sin\theta\cos\theta\bar{C}_{20}\right|$
Mars	$\frac{1}{m\,s^{-2}}\frac{-1}{\rho r}\frac{\partial p}{\partial\theta}$	$0.0225\sin\theta\cos\theta$
Venus	$\frac{1}{m\,s^{-2}}\frac{-1}{\rho r}\frac{\partial p}{\partial\theta}$	$1.1\times10^{-4}\sin\theta\cos\theta$
Titan	$\frac{1}{m\,s^{-2}}\frac{-1}{\rho r}\frac{\partial p}{\partial\theta}$	$4.4\bar{C}_{20}\sin\theta\cos\theta$

(D) Object	$|r_{ref}\Omega^2\sin\theta\cos\theta|$	$\frac{\eta v_\theta}{\rho H^2}$
Mars	$0.017\sin\theta\cos\theta$	3×10^{-3}
Venus	$8.9\times10^{-10}\sin\theta\cos\theta$	4.0×10^{-3} (day)
		or 1.1×10^{-1} (night)
Titan	$7.4\times10^{-5}\sin\theta\cos\theta$	4.8×10^{-4}

Table 3.3: Scale Analysis of Equation 3.7. Units are m s^{-2}. Each term in (A) and (B) corresponds to a term on the left-hand side of Equation 3.18, (C) and (D) to the right-hand side.

θ (degrees)	$\left\|\frac{v_r v_\theta}{r_{ref}}\right\|$	$\left\|\frac{v_\phi v_\theta}{r_{ref}\sin\theta}\right\|$	$\left\|2\Omega v_\phi\cos\theta\right\|$	$\left\|\frac{v_\phi^2}{r_{ref}\tan\theta}\right\|$
10	3.6E-3	5.1E-3	0.014	0.017
20	3.6E-3	2.6E-3	0.013	8.1E-3
30	3.6E-3	1.8E-3	0.012	5.1E-3
40	3.6E-3	1.4E-3	0.011	3.5E-3
50	3.6E-3	1.2E-3	9.0E-3	2.5E-3
60	3.6E-3	1.0E-3	7.0E-3	1.7E-3
70	3.6E-3	9.4E-4	4.8E-3	1.1E-3
80	3.6E-3	9.0E-4	2.4E-3	5.2E-4

Table 3.4: Dominant Terms in Equation 3.18 for Mars case. Units are m s^{-2}.

If geostrophic balance held in the upper atmosphere, this equation would be the same. If I desired to push back the poleward limit, I could also include the $v_\phi^2/r \tan\theta$ curvature term in Equation 3.24 and have a quadratic in v_ϕ for the left hand side.

Returning to the ion-drag term, I decided to estimated the magnitude of the ion-drag term in Equation 3.18 as if the gyrofrequency criterion were satisfied. I set ν_{in} equal to f_{gyro}, then calculated ν_{ni} from the ratio of ion and neutral number densities. The peak ion number density is about 10^{11} m^{-3} at an altitude of 140 km in the example shown in Bougher et al. (2001). This corresponds to a neutral mass density of about 10^{-9} kg m^{-3} or number density for CO_2 of 10^{16} m^{-3} in the MGS ACC PDS data. With these numbers, the ion-drag term is still two orders of magnitude smaller than the Coriolis term.

3.3.3 ϕ component

The first row of Table 3.5 shows the magnitude of each term from Equation 3.19.

The largest latitude-independent term on the left hand side of Equation 3.19 is the 0.01 m s^{-2} $v_r \partial v_\phi/\partial r$ part of the advective term. At polar latitudes the $1/\sin\theta$ part of the advective term is comparable to this. The viscous term is also comparable at all latitudes. The latitude-independent term is dominant for latitudes equatorward of 73°, and at equatorial and mid-latitudes Equation 3.8 is well-approximated by:

$$v_r \frac{\partial v_\phi}{\partial r} = \frac{-1}{r\rho\sin\theta}\frac{\partial p}{\partial\phi} + \frac{\eta}{\rho}\frac{\partial^2 v_\phi}{\partial r^2} \qquad (3.25)$$

If my earlier comments about the correct vertical lengthscale being greater than a scale height are correct, then several other terms should probably be included. However, since I am about to neglect this whole equation, I do not investigate that.

(A) Object	$\frac{v_\phi \Omega}{2\pi}$		$\frac{v_r v_\phi}{H}$		$\frac{v_\theta v_\phi}{r_{ref}}$		$\frac{v_\phi v_\phi}{r_{ref}\sin\theta}$
Mars	1.1×10^{-3}		0.01		8.85×10^{-4}		$\frac{2.95\times10^{-3}}{\sin\theta}$
Venus	1.9×10^{-7}		2.0×10^{-2}		8.1×10^{-5}		$\frac{1.6\times10^{-5}}{\sin\theta}$
Titan	7.3×10^{-5}		1.3×10^{-3}		5.7×10^{-4}		$\frac{2.9\times10^{-3}}{\sin\theta}$

(B) Object	$|2\Omega v_\theta \cos\theta|$	$|2\Omega v_r \sin\theta|$	$\frac{v_\phi v_r}{r_{ref}}$		$\frac{v_\phi v_\theta}{r_{ref}\tan\theta}$
Mars	$4.2 \times 10^{-3} \cos\theta$	$1.4 \times 10^{-4} \sin\theta$	2.9×10^{-5}		$\frac{8.8\times10^{-4}}{\tan\theta}$
Venus	$1.2 \times 10^{-7} \cos\theta$	$2.4 \times 10^{-8} \sin\theta$	1.6×10^{-5}		$\frac{8.1\times10^{-5}}{\tan\theta}$
Titan	$1.8 \times 10^{-4} \cos\theta$	$9.2 \times 10^{-6} \sin\theta$	2.9×10^{-5}		$\frac{5.7\times10^{-4}}{\tan\theta}$

(C) Object	$\frac{-1}{\rho r \sin\theta}\frac{\partial p}{\partial\phi}$		$\frac{\eta v_\phi}{\rho H^2}$	
Mars	$\frac{-1}{\rho r \sin\theta}\frac{\partial p}{\partial\phi}$		1×10^{-2}	
Venus	$\frac{-1}{\rho r \sin\theta}\frac{\partial p}{\partial\phi}$		8.0×10^{-2} (day) or 2.2×10^{0} (night)	
Titan	$\frac{-1}{\rho r \sin\theta}\frac{\partial p}{\partial\phi}$		2.4×10^{-3}	

Table 3.5: Scale Analysis of Equation 3.8. Units are m s^{-2}. Each term in (A) and (B) corresponds to a term on the left-hand side of Equation 3.19, (C) to the right-hand side.

3.3.4   Approximate Equations

Between $\theta = 30°$ and $\theta = 60°$ Equations 3.6 – 3.8 can be approximated by:

$$0 = \frac{-1}{\rho}\frac{\partial p}{\partial r} + \frac{-GM}{r^2} \tag{3.26}$$

$$-2\Omega v_\phi \cos\theta = \frac{-1}{r\rho}\frac{\partial p}{\partial\theta} + g_{eff,\theta} \tag{3.27}$$

$$v_r\frac{\partial v_\phi}{\partial r} = \frac{-1}{r\rho\sin\theta}\frac{\partial p}{\partial\phi} \tag{3.28}$$

The dynamical terms on the left hand sides of Equations 3.27 and 3.28 have about the same magnitude — 0.01 m s^{-2}. Since MGS collected data from a sunsynchronous, near-polar orbit, changes in latitude during a pass are much greater than changes in longitude — at least in the mid-latitudes considered here. On orbit P750 for example, MGS travelled 30° in latitude and 4° in longitude. Even allowing for the effects of the $\sin\theta$ in the denominator of Equation 3.28, changes in pressure along an aerobraking pass are dominated first by changes in vertical position over changes in horizontal position, then by changes in latitude over changes in longitude. Effects of changes in longitude and Equation 3.28 itself can be neglected when deriving pressure profiles from MGS ACC density profiles. The Coriolis term in Equation 3.6 also has a magnitude of 0.01 m s^{-2}. However, since its contribution to the pressure depends on the radial distance travelled, it has a much smaller effect on the total pressure than the Coriolis term in Equation 3.27 and can be neglected from Equation 3.26.

The general conservation of momentum equations are Equations 3.6 – 3.8. The simplest approximation to them are Equations 3.3 – 3.5. The simplest approximation to them that is useful for analysing MGS ACC data is:

$$0 = \frac{-1}{\rho}\frac{\partial p}{\partial r} + \frac{-GM}{r^2} \tag{3.29}$$

$$-2\Omega v_\phi \cos\theta = \frac{-1}{r\rho}\frac{\partial p}{\partial \theta} + g_{eff,\theta} \tag{3.30}$$

The θ component of these equations is in geostrophic balance. The atmosphere itself is not in geostrophic balance, because Equation 3.28 is not dominated by the Coriolis force. I call this situation "quasi-geostrophic" balance. The only unknown quantity affecting the horizontal pressure gradient is the zonal wind, v_ϕ. So, in principle, the horizontal pressure gradients that caused the inbound and outbound estimates of periapsis pressure to differ can be used to solve for v_ϕ. This solution then gives self-consistent pressure and temperature profiles. I later outline a method for doing this in Section 3.7.

3.4   Venus Scale Analysis

Pioneer Venus Orbiter collected many neutral mass spectrometer measurements on passes through the upper atmosphere of Venus. These can be considered as density profiles. As Table 3.1 shows, there are significant differences between the dayside and the nightside of Venus's upper atmosphere. The dayside atmosphere is dominated by CO_2 and has a significantly higher density than the colder nightside O atmosphere (Niemann et al., 1980).

In this case, the radial distance to periapsis altitudes of 150 km is not significantly different from r_{ref} for the gravitational field. I use the radial distance to periapsis altitude as r_{ref}, as discussed in Section 3.2.2.

The ratio of f_{gyro} to ν_{in} is $\sim 3 \times 10^{-5}$ for the Venus dayside and $\sim 1 \times 10^{-3}$ for the nightside, so the ion-drag term has no effect in either case.

3.4.1 r component

For both the dayside and nightside parameters, the second row of Table 3.2 shows the magnitude of each term from Equation 3.17. The dominant term is the 8.3 m s^{-2} gravitational term. The known contributions to the gravitational effects from $\bar{C}_{20}$ and the centrifugal term are much smaller. The largest latitude-independent term on the left hand side is negligible and the largest latitude-dependent term only approaches 10% of 8.3 m s^{-2} gravitational term when $\theta < 1.1° \times 10^{-3}$. So at all latitudes Equation 3.6 is well-approximated by:

$$0 = \frac{-1}{\rho} \frac{\partial p}{\partial r} + \frac{-GM}{r^2} \tag{3.31}$$

3.4.2 θ component

The second row of Table 3.3 shows the magnitude of each term from Equation 3.18. This does vary between day and night. The dominant unknown terms are the $1/\tan\theta$ curvature term and the viscous term at effectively all latitudes. Equation 3.7 is well-approximated by:

$$-\frac{v_\phi^2}{r\tan\theta} = \frac{-1}{\rho r} \frac{\partial p}{\partial \theta} + \frac{\eta}{\rho} \frac{\partial^2 v_\theta}{\partial r^2} \tag{3.32}$$

3.4.3 ϕ component

The second row of Table 3.5 shows the magnitude of each term from Equation 3.19. The dominant unknown term is the viscous term at effectively all latitudes. Equation 3.8 is well-approximated by:

$$0 = \frac{-1}{\rho r \sin\theta} \frac{\partial p}{\partial \phi} + \frac{\eta}{\rho} \frac{\partial^2 v_\phi}{\partial r^2} \tag{3.33}$$

3.4.4   Approximate Equations

For both dayside and nightside, Equations 3.6 – 3.8 can be approximated by:

$$0 = \frac{-1}{\rho}\frac{\partial p}{\partial r} + \frac{-GM}{r^2} \tag{3.34}$$

$$-\frac{v_\phi^2}{r\tan\theta} = \frac{-1}{\rho r}\frac{\partial p}{\partial\theta} + \frac{\eta}{\rho}\frac{\partial^2 v_\theta}{\partial r^2} \tag{3.35}$$

$$0 = \frac{-1}{\rho r\sin\theta}\frac{\partial p}{\partial\phi} + \frac{\eta}{\rho}\frac{\partial^2 v_\phi}{\partial r^2} \tag{3.36}$$

The θ and ϕ components of the conservation of momentum equations are dominated by the effects of viscosity in terms of analysing either the nightside or dayside PVO data. Observed horizontal pressure gradients could, in principle, be related to the second derivative of horizontal wind speed, but this is not a particularly interesting measurement.

Since it is easier to relate horizontal pressure gradients to winds in the Mars and Titan cases than in the Venus case, I do not investigate the Venus case any further.

3.5   Titan Scale Analysis

Cassini will pass through the upper atmosphere of Titan on numerous occasions during its mission. Using a neutral mass spectrometer like PVO, it will also measure density profiles.

In this case, the radial distance to periapsis altitudes of 1000 km is significantly different from the planetary radius. Since $\bar{C}_{20}$ is not known, I use the

radial distance to periapsis altitude as r_{ref} in Equations 3.6 – 3.8, as discussed in Section 3.2.2

The ratio of f_{gyro} to ν_{in} is $\sim 1 \times 10^{-3}$ for Titan, so the ion-drag term has no effect.

3.5.1 r component

The third row of Table 3.2 shows the magnitude of each term from Equation 3.17. The dominant term is the 0.66 m s^{-2} gravitational term as long as $\bar{C}_{20}$ is not unfeasibly large. The largest latitude-independent term on the left hand side is negligible and the largest latitude-dependent term only approaches 10% of 0.66 m s^{-2} gravitational term when $\theta < 2.5° \times 10^{-5}$. So at all latitudes Equation 3.6 is well-approximated by:

$$0 = \frac{-1}{\rho}\frac{\partial p}{\partial r} + \frac{-GM}{r^2} \tag{3.37}$$

3.5.2 θ component

The third row of Table 3.3 shows the magnitude of each term from Equation 3.18. $\bar{C}_{20}$ will be measured by Cassini at the same time as the density profiles, so the dominant unknown term is the $1/\tan\theta$ curvature term for all latitudes more than 20 degrees away from the equator. Equation 3.7 is well-approximated by:

$$\frac{v_\phi^2}{r\tan\theta} = \frac{1}{\rho r}\frac{\partial p}{\partial \theta} \tag{3.38}$$

3.5.3 ϕ component

The third row of Table 3.5 shows the magnitude of each term from Equation 3.19. The dominant unknown terms are two parts of the advective term and the viscous term. Equation 3.8 is well-approximated by:

$$v_r \frac{\partial v_\phi}{\partial r} + \frac{v_\phi}{r \sin \theta} \frac{\partial v_\phi}{\partial \theta} = \frac{-1}{\rho r \sin \theta} \frac{\partial p}{\partial \phi} + \frac{\eta}{\rho} \frac{\partial^2 v_\phi}{\partial r^2} \tag{3.39}$$

3.5.4 Approximate Equations

Equation 3.39 is quite intractable. However, some of Cassini's orbits will be sufficiently close to polar that the change in pressure due to changes in longitude will be negligible. In those cases, Equations 3.6 – 3.8 can be approximated by:

$$0 = \frac{-1}{\rho} \frac{\partial p}{\partial r} + \frac{-GM}{r^2} \tag{3.40}$$

$$\frac{v_\phi^2}{r \tan \theta} = \frac{1}{\rho r} \frac{\partial p}{\partial \theta} \tag{3.41}$$

Since Equation 3.41 is similar in form to the case of cyclostrophic balance, I call this situation "quasi-cyclostrophic" balance.

3.6 Summary of Simplified Equations

For each of these three cases, the approximation to the ϕ-component of Equation 3.1 (Equation 3.8) contains spatial derivatives of the wind velocity. It is much easier to deal with equations which contain the undifferentiated wind speed, so I only consider

near-polar orbits for which the change in pressure along a leg due to changes in longitude are negligible compared to those due to changes in latitude.

For the quasi-geostrophic case of Mars, my approximate equations are:

$$\frac{1}{\rho}\frac{\partial p}{\partial r} = -\frac{GM}{r^2} \tag{3.42}$$

$$2\Omega v_\phi \cos\theta = \frac{1}{\rho r}\frac{\partial p}{\partial \theta} - g_{eff,\theta} \tag{3.43}$$

For the quasi-cyclostrophic case of Titan, my approximate equations are:

$$\frac{1}{\rho}\frac{\partial p}{\partial r} = -\frac{GM}{r^2} \tag{3.44}$$

$$\frac{v_\phi^2}{r\tan\theta} = \frac{1}{\rho r}\frac{\partial p}{\partial \theta} - g_{eff,\theta} \tag{3.45}$$

The importance of latitudinal changes in pressure can be gauged by comparing the inbound and outbound estimates for periapsis pressure where these estimates assume that pressure gradients and gravity are the only forces acting. If they are identical, then latitudinal changes in pressure are negligible. If they are very different, then latitudinal changes in pressure are significant. I define E as the ratio of the difference of these two periapsis pressure estimates to their mean. $E = 0$ corresponds to the case of negligible latitudinal effects, $E \neq 0$ corresponds to the case of significant latitudinal effects. Appendix E outlines a method for estimating E, with some rather sweeping assumptions to deal with the effects of changing latitude on the trigonometric terms. The results are that $E \sim 0.2$ for the MGS ACC case at Mars and $E \sim 0.05$ for the Cassini INMS case at Titan. The martian estimate is

similar to my measurement of $E \sim 0.5$ in Section 3.1. Detecting this effect on Titan in the near-polar orbits of the Cassini data might be possible, because the INMS instrument has high performance characteristics, but the ever-changing geometry of the flybys will be a major complication.

3.7 "Balanced Arch" Technique for Estimating Wind Speed

In the quasi-geostrophic balance case, the zonal wind speed can be estimated as follows. The conservation of momentum equations between $\theta = 30°$ and $\theta = 60°$ are approximated as:

$$\frac{\partial p}{\partial r} = \rho g_{eff,r} \tag{3.46}$$

$$\frac{\partial p}{\partial \theta} = \rho r g_{eff,\theta} + 2\rho r \Omega v_\phi \cos\theta \tag{3.47}$$

Unknowns are v_ϕ and p as functions of r and θ. A zeroth order estimate of periapsis pressure from the inbound density profile, neglecting winds, is:

$$\int_{entry}^{peri} \rho g_{eff,r} dr + \int_{entry}^{peri} \rho r g_{eff,\theta} d\theta \tag{3.48}$$

Where the integration path is along the flight path. If v_ϕ is known, this estimate can be improved so that it gives the correct periapsis pressure by adding it to an offset term:

$$\int_{entry}^{peri} 2\Omega \rho r v_\phi \cos\theta d\theta \tag{3.49}$$

Similar expressions exist for the outbound leg, with exit replacing entry.

If I assume that v_ϕ is uniform, then it can be moved outside the integration and the offset term becomes:

$$v_\phi \int_{entry}^{peri} 2\Omega\rho r \cos\theta d\theta \tag{3.50}$$

Periapsis pressure is therefore given by both the following:

$$\int_{entry}^{peri} \rho g_{eff,r} dr + \int_{entry}^{peri} \rho r g_{eff,\theta} d\theta + v_\phi \int_{entry}^{peri} 2\Omega\rho r \cos\theta d\theta \tag{3.51}$$

$$\int_{exit}^{peri} \rho g_{eff,r} dr + \int_{exit}^{peri} \rho r g_{eff,\theta} d\theta + v_\phi \int_{exit}^{peri} 2\Omega\rho r \cos\theta d\theta \tag{3.52}$$

Equating these two expressions and rearranging them to solve for v_ϕ gives:

$$v_\phi = \frac{\left(\int_{entry}^{peri} \rho g_{eff,r} dr + \int_{entry}^{peri} \rho r g_{eff,\theta} d\theta\right) - \left(\int_{exit}^{peri} \rho g_{eff,r} dr + \int_{exit}^{peri} \rho r g_{eff,\theta} d\theta\right)}{\int_{exit}^{peri} 2\Omega\rho r \cos\theta d\theta - \int_{entry}^{peri} 2\Omega\rho r \cos\theta d\theta} \tag{3.53}$$

Which can be solved for v_ϕ using the density profiles and Ω. This solution for v_ϕ represents a characteristic zonal wind speed in the region spanned by the areobraking pass. It is affected by all the neglected terms omitted from Equations 3.29 – 3.30. I call this result the "derived zonal wind speed" to emphasize that it is averaged over an unrealistically large spatial extent.

This technique, as currently implemented, satisfies an integrated version of Equation 3.30 and gives a single estimate of v_ϕ for the entire pass. By comparing latitudinal pressure gradients at every altitude on the pass and using the unintegrated Equation 3.30, a vertical profile of zonal wind speed can be derived. I leave this for future work.

With this zonal wind estimate, pressure profiles which are consistent at periapsis can be derived by substituting the value for v_ϕ into Equations 3.29 – 3.30 and then integrating in both r and θ with the usual boundary condition at the top of the atmosphere.

Uncertainties on the zonal wind estimate are calculated from the formal uncertainties in the various terms in Equation 3.53. To perform the integrations, I used a simple first order routine, stated below in Equation 3.54. Errors are propagated formally through the summation. The simple integration routine enables simple error calculations.

$$\int_{x_{start}}^{x_{stop}} y\left(x\right) dx = \sum_{i=0}^{i=n-1} y\left(x_i\right)\left(x_{i+1} - x_i\right) \tag{3.54}$$

ACC density measurements are evenly distributed in time, not r or θ, so not all dr are the same. Uncertainties in the pressure profile are also calculated by formally propagating errors through a first order summation for the integrations in Equation 3.51. These formal uncertainties do not consider any effects of the terms neglected in arriving at Equations 3.29 – 3.30. Monte Carlo simulations could be used to estimate the effects of these neglected terms on the uncertainty in the derived wind speed.

The analogous procedure for the case of cyclostrophic balance is as follows:

$$v_\phi^2 = \frac{\left(\int_{entry}^{peri} \rho g_{eff,r} dr + \int_{entry}^{peri} \rho r g_{eff,\theta} d\theta\right) - \left(\int_{exit}^{peri} \rho g_{eff,r} dr + \int_{exit}^{peri} \rho r g_{eff,\theta} d\theta\right)}{\int_{exit}^{peri} \frac{\rho r}{\tan\theta} d\theta - \int_{entry}^{peri} \frac{\rho r}{\tan\theta} d\theta} \tag{3.55}$$

Unlike the quasi-geostrophic case, the direction of the zonal wind is not known from this solution, only its magnitude. The direction must be inferred from other information.

I call this technique for measuring wind speeds using two simultaneous

density profiles the "Balanced Arch" technique to emphasize (a) the need to balance one leg of the aerobraking pass against the other and (b) the arched, non-vertical shape of each leg of the aerobraking pass.

3.8   Validation of "Balanced Arch" Technique

This proposed technique should be tested before results from it are accepted. The best validation would be to have measurements of winds, densities, and pressures in the martian upper atmosphere with excellent spatial coverage and resolution, apply this technique to the densities corresponding to an aerobraking pass, and test whether the derived wind bears any resemblance to the actual measured winds. Unfortunately, such a dataset does not exist. I tried a two-stage approach for validation instead. The first stage was to test this technique on a very simple model of an atmosphere which satisfies perfectly most of the assumptions made in deriving Equations 3.29 – 3.30 perfectly. The second stage was to test this technique on a general circulation model of an atmosphere which does not neglect these terms.

3.8.1   Test on a Simple Atmosphere

To test this technique I created an idealized atmosphere that satisfies Equation 3.1. It is isothermal (150K), has $v_r = 0, v_\theta = 0$, and $v_\phi =$ constant everywhere, includes rotation at martian angular speeds, has a martian GM, a uniform radius equal to r_{ref}, and spherically symmetric $\underline{g_{grav}}$ equal to GM/r_{ref}^2. Ω, GM, and r_{ref} are as tabulated in Table 3.1. Periapsis latitude is 45°N and periapsis altitude is 120 km. The aerobraking profile passes through the top of the atmosphere at 30°N and 150 km and its altitude has a quadratic dependence on latitude, as discussed in Appendix E.

The initial condition for the integration equates the pressure at the top of the atmosphere to $\rho g H$, where H is the density scale height. It is calculated from

an exponential best-fit ($\ln \rho = \ln \rho_0 - r/H$) to the first ten kilometres in altitude of the density profile. The r range of ten kilometres is chosen as a reasonable *a priori* estimate for the scale height, which is actually 7.6 km. As usual, this estimate for the top of the atmosphere scale height assumes an isothermal atmosphere (which happens to be correct in this idealized model) *and* ignores the effects of latitudinal changes on the pressure. Equation E.17 shows how a later solution for v_ϕ could be used to account for latitudinal effects, which could be significant on rapidly-rotating planet or one with very fast zonal wind speeds, but I do not worry about this in the current work. Errors in this boundary condition become negligible in the pressure profile at lower altitudes.

Extracting a density profile from this model atmosphere, and then applying the Balanced Arch technique of Equation 3.53 yields the correct, *i. e.* the one specified in the simulation, result for the zonal wind speed. Changing the uniform zonal wind speed, the uniform temperature, periapsis latitude, latitudinal width of the pass, periapsis altitude, or the altitude of the top of the atmosphere do not affect the technique, it still gives the correct result for the applied uniform zonal wind field. The latitudinal limits on the technique are due to neglected terms becoming important. In this idealized kind of simulation the neglected terms are equal to zero, so the limits do not occur.

Next, I set the zonal wind speed equal to 100 m s^{-1} at periapsis and 0 m s^{-1} at the top of the atmosphere. Zonal wind speed was constant and uniform in the atmosphere, except across an artificial discontinuity placed at a fixed altitude. Increasing the boundary altitude between periapsis and the top of the atmosphere led to a high derived zonal wind speed, and decreasing it led to a low derived zonal wind speed. For each set of periapsis altitude and latitude, top of the atmosphere altitude, and temperature, I varied the boundary altitude to find that which gave a measured zonal wind speed of 50 m s^{-1}, *i. e.* the mean of the two extreme values. The boundary altitude always remained within 2 or 3 km of periapsis, so I conclude that this technique derives zonal wind speeds that are heavily weighted to periapsis

altitude.

This is probably due to the weighting by $1/\rho$ in Equation 3.30. The greatest contribution to changes in p, which is what is needed to fix the periapsis pressure mismatch and constrain v_ϕ, occurs when density is the highest, which is at periapsis. Altitudes where the change in latitude is greatest per unit change in altitude are also favoured. With a parabolic aerobraking pass, this again causes periapsis to have the largest effect on the derived zonal wind speed.

I then set the zonal wind speed equal to 100 m s^{-1} at periapsis and 0 m s^{-1} at the furthest latitudes. Zonal wind speed was constant in the atmosphere, except across two artificial discontinuities placed at fixed latitudes. Zonal wind speed was symmetric about periapsis latitude. Moving the boundaries close to the periapsis latitude led to a low derived zonal wind speed, moving them away from the periapsis latitude led to a high derived zonal wind speed. The boundary latitude was always about 25% of the way from periapsis to the furthest latitudes. For MGS's aerobraking passes this means that the boundary latitude intersects the parabolic profile within 2 to 3 km above periapsis.

Derived zonal wind speeds are weighted towards wind speeds at the periapsis latitude and are heavily weighted to those at the periapsis altitude.

3.8.2   MTGCM Testing

Section 3.8.1 shows that zonal wind speeds can be measured using this technique in an atmosphere that satisfies perfectly the assumptions leading to Equations 3.29 – 3.30. However, in a real atmosphere the neglected terms do not vanish and I tried to validate this technique on a more realistic atmospheric model. Since the effects of zonal winds on pressure profiles are predicted to be greatest on Mars, and since the data analysis sections of this dissertation (Chapter 4) concentrate exclusively on martian data, I wished to use a more detailed model of the martian atmosphere.

General Circulation Models include much of the physics that is neglected by imposing quasi-geostrophic balance and are more realistic depictions of the mean state of an atmosphere. I note that they are climate, not weather, models, and so actual observations contain additional noise and small-scale disturbances that cannot be included in the GCM. I planned to extract density profiles from GCM simulations representative of those from MGS aerobraking, apply this technique to measure the zonal wind speed, and compare the derived zonal wind speed to the actual zonal wind speed in the simulation. However, when I began working with the data from simulations, I found problems with the conservation of momentum. The simulations did not appear to be satisfying what I thought were the correct conservation equations, Equations 3.6 – 3.8. After some experimentation I discovered a problem with the simulations. They do not exactly conserve the horizontal components of momentum. The size of the error is comparable to the Coriolis term that I expect to retain as the only dynamical term. The reason for this problem is a simple one; the simulations, which require large quantities of supercomputing time, were not instructed to run for long enough to reach a perfect steady state. They were instructed to consider steady state reached when they were actually somewhat away from a perfect steady state. Additional simulations are in progress which will more closely approach a perfect steady state and thus have reduced errors in the momentum equations. These results are not yet available, but will be discussed in later work.